



## Construction of CDs/CdS photocatalysts for stable and efficient hydrogen production in water and seawater

Cheng Zhu<sup>1</sup>, Chang'an Liu<sup>1</sup>, Yijun Fu, Jin Gao, Hui Huang\*, Yang Liu\*, Zhenhui Kang\*

Jiangsu Key Laboratory for Carbon-Based Functional Materials & Devices, Institute of Functional Nano & Soft Materials (FUNSOM), Soochow University, 199 Ren'ai Road, Suzhou, 215123, Jiangsu, PR China



### ARTICLE INFO

#### Keywords:

Carbon dots/cadmium sulfide hybrid  
Photocatalytic hydrogen production  
Water and seawater  
High efficiency and stability  
Improved charge transport and separation

### ABSTRACT

Photocatalytic hydrogen production on semiconductors has been intensively researched in the past years, yet it still lacks research on efficient and stable photocatalysis in seawater. In this paper, with cadmium sulfide (CdS) as a sample photocatalyst and carbon dots (CDs) as cocatalyst, we fabricated a series of CDs/CdS composites serving as efficient hydrogen production photocatalysts in both water and seawater. In this case, the optimal CDs/CdS-S composites (nanosheet with cocatalyst content of 0.01 g<sub>CdS</sub>/g<sub>catalyst</sub>) exhibit prominent H<sub>2</sub> production rate of 4.64 mmol h<sup>-1</sup> g<sup>-1</sup> (6.70 mmol h<sup>-1</sup> g<sup>-1</sup>, water) and AQE of 11.8% (19.3%, water) under 420 nm light irradiation in seawater, which are about 265 and 169 (78 and 77, water) times of those of the non-modified irregular CdS in seawater, respectively. The excellent activity and stability are attributed to the competency of CDs that not only dramatically improves the charge separation efficiency, but also plays indispensable role in resisting the distraction from various ionic components in seawater. We hope our work can provide a feasible perspective for constructing high-efficient photocatalyst towards practical applications.

### 1. Introduction

Inspired by natural photosynthesis, hydrogen production from solar water splitting has prompted keen interests since the past decades, which can date back to 1972 when TiO<sub>2</sub> was reported for photo-electrical chemical water decomposition [1–5]. Due to the foreseeable possibility for converting the inexhaustible solar energy and most abundant natural resource (water/seawater) into chemical fuels in large-scale ways, tremendous efforts have been devoted to developing various semiconductors as efficient photocatalysts especially those competent to utilize visible light ( $\lambda \geq 420$  nm) that accounts for about 43% of the solar spectrum [6–12]. Chalcogenide semiconductors are considered as good candidates for photocatalytic hydrogen production owing to the intrinsic merits such as suitable band gap, strong light response, good thermal stability and high-activity [6,7]. Particularly, cadmium sulfide (CdS) is one of the high-profile chalcogenide photocatalysts on account of its relatively narrow band gap (normally is 2.40 eV), which is capable of effectively making use of visible light [13,14].

Recent studies have pointed out photocatalytic activity of CdS is closely related to its topological structure with different parameters like crystal structure, specific surface area and particle size [15,16]. So far,

numerous methods are reported to synthesize CdS nanocrystals with multifarious shapes [17–20], which bring further influences such as the band structure, charge separation efficiency, charge transfer process and interfacial reaction. Despite the fact that noble metal based cocatalysts (such as Pt, and Ru) have achieved satisfactory results, considering the perspective of budget and environment, low-cost and eco-friendly cocatalysts nonetheless would be more favored [21–23]. Furthermore, nearly all current studies are only focused on the photocatalysis in water, hence it still requires to divert our lens to the photocatalytic activity in the most abundant natural seawater, which is more ideal for the future applications for its vast and inexhaustibility. Up to date, however, there are only a few reports on stable photocatalysis systems for seawater splitting [24–27]. Due to the vast quantity of ionic components and impurities in seawater, the activity and stability of the photocatalysts are seriously affected, restricting the large-scale applications of solar seawater splitting [28,29]. Therefore, it is indispensable to study the photocatalytic activity of CdS composites with respect to high activity and stability, providing competent candidates for practical solar seawater splitting.

Carbon dots (CDs) with high specific surface area can be anchored with abundant surface functional moieties, such as COOH, OH, and C = O, by facile treatment [30–32]. Additionally, known as fine

\* Corresponding authors.

E-mail addresses: [hhuang0618@suda.edu.cn](mailto:hhuang0618@suda.edu.cn) (H. Huang), [yangl@suda.edu.cn](mailto:yangl@suda.edu.cn) (Y. Liu), [zhkang@suda.edu.cn](mailto:zhkang@suda.edu.cn) (Z. Kang).

<sup>1</sup> These authors contributed equally.

electron acceptors, the unique electron reservoir property, electron transfer property, low-cost, non-toxicity and good stability have made CDs as a favorable cocatalyst for photocatalysis [33–36]. Though graphene has been widely researched as excellent cocatalysts in CdS photocatalytic systems [37,38], ~5 nm nano-sized CDs can be easily functionalized and loaded on catalysts which tends to form a great deal of well-dispersed reduction sites to boost the charge separation and hydrogen production. Moreover, CDs can be prepared by simple electrochemical etching method, which is facile, productive and cheap.

In this work, we report the synthesis of a series of CDs/CdS nanocomposites with four representative morphologies, including nanorods, nanosheets, nanospheres and irregular particles. The desired composites exhibit outstanding photocatalytic activity for hydrogen production in both water and seawater. For CdS, the hydrogen production rate decreases in the order: nanorods > nanosheets > nanospheres > irregular particles. In contrast, the hydrogen production rate of CDs/CdS declines in the order: nanosheets > nanorods > nanospheres > irregular particles. In particular, the optimal CDs/CdS composites exhibit supreme hydrogen production rate of  $4.64 \text{ mmol h}^{-1} \text{ g}^{-1}$  ( $6.70 \text{ mmol h}^{-1} \text{ g}^{-1}$ ) and apparent quantum efficiency of 11.8% (19.3%) in seawater (water). These experimental results verify: 1) the introduction of CDs as cocatalysts drastically improves the charge separation efficiency; 2) CDs can enhance the catalytic stability of CdS in water and seawater; 3) the consolidation of cocatalyst and morphology is a doable methodology unto high-efficiency.

## 2. Experimental section

### 2.1. Synthesis of the samples

#### 2.1.1. Synthesis of CDs

CDs were produced by a typical electrolytic method [31]. Briefly, two graphite rods (diameter 6.15 mm and length 15 cm) were used as anode and cathode respectively in an electrolytic bath of ultrapure water ( $18.2 \text{ M cm}^{-1}$ , 1000 mL). Then, 30 V was applied across the electrodes using a direct current power supply until the colorless electrolyte changed to a dark solution. Afterwards, the solution was filtered with a slow-speed quantitative filter paper, and the resultant solution was centrifuged at 8000 rpm for 30 min to remove the precipitated graphite oxide and big graphite particles. Finally, the CDs powder was obtained by freeze-drying.

#### 2.1.2. Synthesis of CDs/CdS nanorods (CDs/CdS-R)

In a typical synthetic process, 4.63 g of  $\text{CdCl}_2 \cdot 2.5\text{H}_2\text{O}$ , 4.63 g of  $\text{NH}_2\text{CSNH}_2$  and different quantities of CDs (0.001, 0.005, 0.01, 0.02, and 0.03 g) were dissolved in 60 mL of ethylenediamine (en) under magnetic stirring to form a mixture. After that, the mixture was transferred into a 100 mL Teflon-lined autoclave and maintained at  $160^\circ\text{C}$  for 36 h. Next, the autoclaves were cooled down to room temperature naturally, and the yellow precipitates were collected by centrifugation and rinsed several times with ultrapure water and absolute alcohol alternately. Finally, the final product was dried at  $60^\circ\text{C}$  for 10 h. The pure CdS nanorods were synthesized in the same process without adding CDs.

#### 2.1.3. Synthesis of CDs/CdS nanosheets (CDs/CdS-S)

CDs/CdS-S was synthesized in the following procedure: 0.32 g of sulfur powder and 0.37 g of  $\text{CdCl}_2 \cdot 2.5\text{H}_2\text{O}$  were dissolved in 60 mL diethylenetriamine (DETA) and CDs powder was then added into the mixture. Ultrasonic dispersion was required for at least 30 min to get a homogeneous solution. After that, the mixture was transferred into a 100 mL Teflon-lined stainless-steel autoclave, and kept at  $80^\circ\text{C}$  for 72 h. After cooling down to room temperature, a yellow product was collected by centrifugation. Afterwards, the product was washed by ethanol and distilled water respectively for several times. Finally, the samples were dried at  $60^\circ\text{C}$  in a vacuum drying oven to get yellow

powder. The pure CdS nanosheets were synthesized in the same process without the addition of CDs.

#### 2.1.4. Synthesis of CDs/CdS nanospheres (CDs/CdS-N)

The CDs/CdS-N were synthesized by a facile hydrothermal treatment. In detail, 0.11 g of  $\text{Cd}(\text{CH}_3\text{COO})_2 \cdot 2\text{H}_2\text{O}$  and CDs powder were added into 40 mL DMSO with vigorously stirring for 30 min. Then, the mixture was transferred into a 50 mL Teflon-lined autoclave. The autoclave was sealed and heated at  $180^\circ\text{C}$  for 12 h. The products were collected and washed three times with deionized water and ethanol after the autoclave was cooled to room temperature. After that, the samples were dried at  $60^\circ\text{C}$  in a vacuum drying oven. The pure CdS nanospheres were synthesized in the same process without adding CDs.

#### 2.1.5. Synthesis of the irregular CDs/CdS particles (CDs/CdS-I)

The irregular CDs/CdS-I were also synthesized by hydrothermal treatment. In typical procedure: 0.53 g  $\text{Cd}(\text{CH}_3\text{COO})_2 \cdot 2\text{H}_2\text{O}$ , 0.49 g L-cysteine and CDs powder were well-dispersed into 50 mL triethanolamine (TEA). Then, the mixture was transferred into a 100 mL Teflon-lined autoclave. The autoclave was sealed and heated at  $180^\circ\text{C}$  for 24 h. After cooling to room temperature, the products were collected and washed three times with deionized water and ethanol. The final samples were dried at  $60^\circ\text{C}$  in a vacuum drying oven. The pure irregular CdS particles were synthesized in the same process without the addition of CDs.

## 2.2. Characterization

All the regents are purchased from Sigma-Aldrich and Adams-beta<sup>®</sup> without further purification. Transmission electron microscopy (TEM), high-resolution transmission electron microscopy (HRTEM) and energy dispersive x-ray analysis (EDX) were measured by using a FEI-Tecnai F20 transmission electron microscope with an accelerating voltage of 200 kV. The size distribution was measured by dynamic light scattering (DLS) on a Malvern ZEN3690. The atomic force microscope (AFM) was used to determine the particle size of CDs. Scanning electron microscope (SEM) was applied to characterize the morphology of the samples. The Fourier transform infrared (FTIR) spectra of the samples were acquired from a Hyperion spectrophotometer (Bruker) at the scan range of  $400\text{--}4000 \text{ cm}^{-1}$ . UV/VIS/NIR spectrophotometer (Lambda 750, PerkinElmer) was employed to acquire the UV-Vis absorption spectra. Raman spectra were collected by using a HR 800 Raman spectroscope (J Y, France) with a 20 mW air-cooled argon ion laser (633 nm) as the excitation source. Powder X-ray diffraction (XRD) was carried out to characterize the crystal structure of the as-prepared products by using a PIXcel3D X-ray diffractometer (Empyrean, Holland Panalytical) with Cu K radiation. X-ray photoelectron spectroscopy (XPS) measurements were conducted on a KRATOS Axis ultra-DLD X-ray photo-electron spectroscope with a monochromatic Al K X-ray source. All the electrochemical measurements were conducted on a CHI 920C workstation (CH Instruments, Shanghai, China) using a standard three-electrode system, of which a platinum wire is used as the counter electrode, a saturated calomel electrode (SCE) as the reference electrode and a glass carbon (GC) electrode as working electrode. The photoresponse-time curves were obtained at open circuit potential (OCP) with a 300 W Xe-lamp as the light source. Electrochemical impedance spectra (EIS) measurements were carried out at open circuit potential as well, with a frequency range from 1 MHz to 0.01 Hz and an AC voltage amplitude of 5 mV in ultrapure water.

## 2.3. Water splitting test

The water splitting tests were conducted in both water and seawater, respectively. The seawater was obtained from China Yellow Sea  $33^\circ17'58.0''\text{N}$   $120^\circ47'18.7''\text{E}$  and simply filtered before use. Typically, 40 mg photocatalysts were dispersed in 80 mL pure water (seawater)

with 8 mL lactic acid. Then the homogenous solution was transferred to a Pyrex glass photoreactor (equipped with a flat window at the top for illumination, and a magneton at the bottom), which was connected to a closed gas-circulation system. Afterwards, the system was degassed to completely remove air. The temperature of the mixed liquor was maintained at 25 °C by cyclic water installation during the photocatalytic reaction. Under constant stirring, the suspension was irradiated by an AM 1.5G solar simulator (MICROSOLAR 300, Beijing Perfectlight Co. Ltd., People's Republic of China). To detect the gas production, a gas chromatograph (GC-7890) set up with a 5 Å molecular sieves column and a thermal conductivity detector (TCD) was utilized. Nitrogen (N<sub>2</sub>) was used as the carrier gas with the flow rate of 30 mL min<sup>-1</sup>.

#### 2.4. Calculation of apparent quantum efficiency (AQE) under ambient pressure

For apparent quantum efficiency (AQE) valuations, 10 mg photocatalyst, 18 mL ultrapure water (seawater), 2 mL lactic acid and a stir bar were put into a quartz photo-reactor vial with a total volume of 60 mL. Afterwards, the system was sealed to avoid gas leakage. The upper 40 mL space is remained to gather the produced hydrogen. In order to reduce the pressure impact on photocatalytic activity, measurement was conducted with an interval of 1 h. After each measurement, the vial was opened and resealed to remove residual hydrogen. The vials were set under constant stirring with light-emitting diode (LED) ( $\lambda_0 = 420, 460$  or 500 nm) as the light sources. A GC-7890 gas chromatograph (GC) set up with a thermal conductivity detector (TCD) and 5 Å molecular sieves column was employed for the evolved gas detection. Nitrogen was used as the carrier gas with a flow rate of 30 mL min<sup>-1</sup>.

The average intensity of irradiation was determined to be 10.2 mW·cm<sup>-2</sup> by an ILT 950 spectroradiometer (International Light Technologies) and the irradiation area was 7 cm<sup>2</sup>. The number of incident photons (N) is calculated by Eq. (1).

$$N = \frac{E\lambda}{hc} \quad (1)$$

In Eq. (1), E is the average intensity of irradiation,  $\lambda$  stands for the wavelength of the irradiation,  $h$  represents the Planck constant and  $c$  is the speed of light.

The quantum efficiency is calculated from Eq. (2).

$$AQE = \frac{2 \times \text{number of evolved H}_2 \text{ molecules}}{\text{number of incident photons}} \times 100\% \quad (2)$$

### 3. Results and discussion

#### 3.1. Characterization of CDs and composite photocatalysts

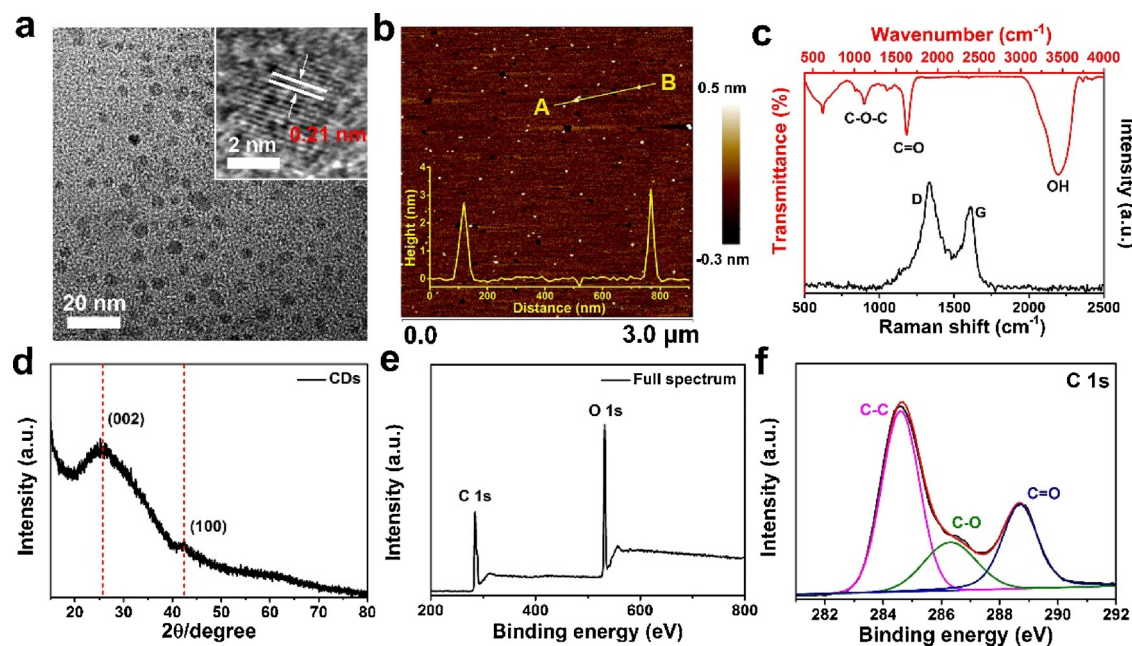
Fig. 1a shows the TEM and high-resolution TEM (HRTEM) images taken from monodispersed CDs and a single CD, respectively. It is clear that CDs are torispherical nanoparticles with diameter from approximately 2 to 6 nm. The DLS diagram (Fig. S1) also verifies the size distribution of CDs. As shown in the inset of Fig. 1a, the lattice spacing of 0.21 nm accords with the (100) lattice plane of graphitic carbon. AFM image also exhibits the uniform distribution of CDs (Fig. 1b), where the inserted coordinate system indicates that the height of measured CDs along line AB located within the size distribution. Raman spectrum of CDs (Fig. 1c) has two prominent peaks centered at around 1320 and 1590 cm<sup>-1</sup>, which are ascribed to the D band of the sp<sup>3</sup>-banded carbon atoms in disordered graphite and G band from in-plane vibration of sp<sup>2</sup> carbon, respectively. The functional groups are indicated in FTIR spectrum (Fig. 1c), where the peaks located at 3440, 1650 and 1120 cm<sup>-1</sup> are assigned to the stretching vibration of OH, C=O, and C—O—C, respectively. [34] XRD pattern of CDs (Fig. 1d) shows two

broad peaks at around 26° and 43°, well corresponding to the (002) and (100) planes of graphitic carbon. The full XPS spectrum suggests CDs only have C and O elements (Fig. 1e). The C 1 s high-resolution spectrum of CDs can be fitted into three peaks, where the peak at 284.6 eV is assigned to C—C/C=C, while the binding energies at 286.3 and 288.3 eV can be attributed to the C—O and C=O bonds, respectively. [34]

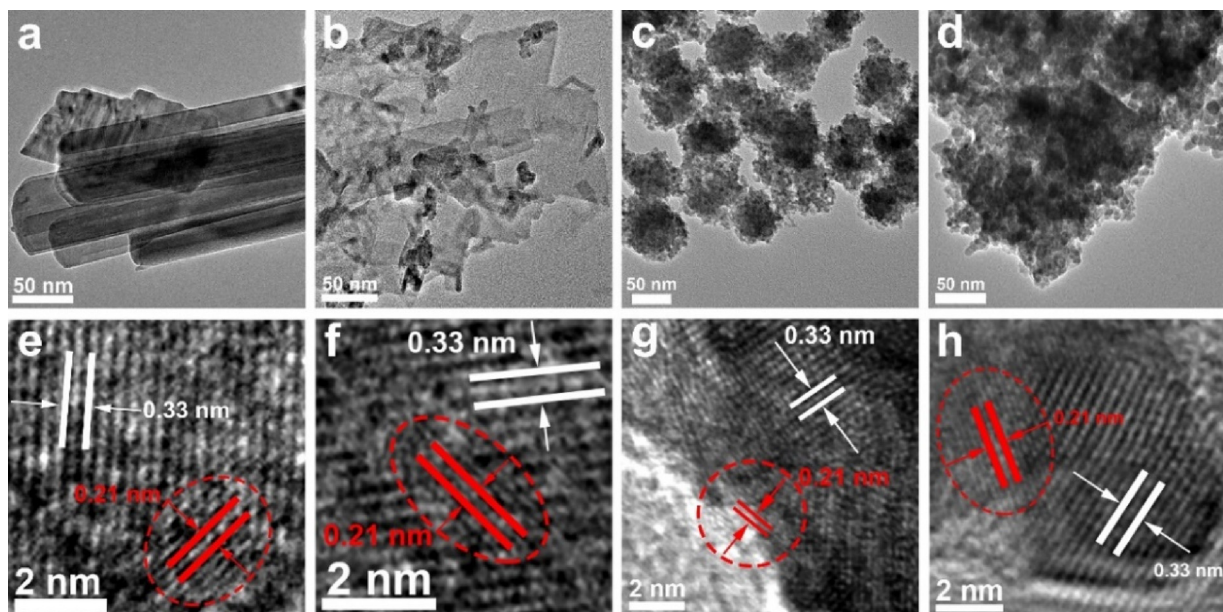
Four typical morphologies of CDs/CdS composites were synthesized through hydrothermal treatment with different sulfur sources and solvents. The morphologies of CDs/CdS composites were investigated by TEM as shown in Fig. 2. Fig. 2a shows typical rod-like CDs/CdS-R with a diameter from 50 to 60 nm. Fig. 2b displays CDs/CdS-S are nanosheets with thin layers. CDs/CdS nanospheres (Fig. 2c) exhibit approximately uniform size (diameter around 60 nm) and distribution with vesicle-like structure. Unlike the others, irregular CDs/CdS-I composites are big bulks without characteristic morphological structure (Fig. 2d). TEM image of CDs/CdS-I reveals the presence of closely aggregated nanoparticles with irregular shape. The corresponding HRTEM images are shown in Fig. 2e–h, where the lattice spacing of 0.21 nm corresponds to the (100) plane of CDs (highlighted in a red dashed circle) while 0.33 nm represents the (002) plane of hexagonal phase or (111) plane for cubic phase CdS [20,34,39]. The corresponding EDX mappings shown in Figs. S2–S5 manifest uniformly distributed S, Cd, C, and O elements in these composite photocatalysts, suggesting CDs are evenly integrated with CdS. Note both C and O come from CDs. The pure phase CdS with different morphologies are regarded as contrastive samples, which are synthesized in the same conditions only in absence of CDs. TEM and HRTEM images of pure phase CdS with four morphologies are provided in Fig. S6, showing identical morphologies as CDs/CdS composites.

Fig. S7 provides the XPS full spectra of CDs/CdS composites with different morphologies. Only C, S, O, Cd are detected in the full spectra. As shown in Fig. 3a, the fuzzy C 1 s spectra have indicated the chemical states of carbon, which still can be deconvoluted into three peaks at around 284.6, 286.3 and 288.3 eV, corresponding to C—C, C—O and C=O bonds. The consequence results from the low loading content of CDs, yet it is still consistent with XPS C 1 s spectrum of CDs (Fig. 1f). The core level S 2p spectra demonstrate two peaks of S 2p<sub>3/2</sub> and S 2p<sub>1/2</sub> with a splitting of 1.2 eV, which locate at about 160.3 and 161.5 eV respectively (Fig. 3b), stemming from the valence state of S<sup>2-</sup> in CdS [34,40,41]. In the meantime, the fitted peaks of the Cd 3d<sub>5/2</sub> and Cd 3d<sub>3/2</sub> centred at 403.9 and 410.7 eV (with a splitting energy of 6.8 eV) finely indicate Cd<sup>2+</sup> in CdS (Fig. 3c) [34,40]. An atomic ratio of approximately 1:1 is obtained for Cd and S, which further verifies the CdS phase in the composites.

Based on Fig. 4a, XRD diffraction patterns of CDs/CdS-R and CDs/CdS-S samples can be indexed as (100), (002), (101), (102), (110), (103), (112) and (202) planes of the hexagonal phase of the wurtzite CdS structure (JCPDS No. 41-1049) since the intensity of (103) plane can be only assigned to the hexagonal phase of CdS. Further observation visualizes that the (102) diffraction peak almost vanishes and (103) diffraction peak becomes very weak for CDs/CdS-I, indicating CDs/CdS-I samples contain both cubic and hexagonal phases. By contrast, the diffraction pattern of CDs/CdS-N presents four characteristic peaks at  $2\theta = 26.5^\circ, 30.7^\circ, 44.0^\circ$  and  $52.0^\circ$  merely, which belong to (111), (200), (220) and (311) reflections of the cubic phase CdS (JCPDS 075–1546). In general, the strong and narrow diffraction peaks in XRD patterns point to a high crystallinity of the samples. However, both CDs/CdS-I and CDs/CdS-N samples have several broad diffraction peaks attributed to the fragmentary formation of CdS nanostructures, demonstrating the aggregation of small CdS particles with poor crystallinity. The XRD patterns of pure phase CdS are the same with those from CDs/CdS composites (Fig. S8), indicating that the incorporation of CDs doesn't change the crystal structure of CdS. Note no characteristic peaks of CDs was identified in the XRD patterns because of the low loading content of CDs in the composites as well as the overlapping of



**Fig. 1.** (a) Typical TEM image of CDs particles; inset is the HRTEM image of a single CD. (b) Representative height-mode AFM topography image of CDs on silicon substrate; inset shows the height profile along line AB. (c) Raman (black curve) and FTIR spectra (red curve) of CDs. (d) XRD pattern of CDs. (e) XPS full scan spectrum of CDs. (f) High-resolution C 1 s XPS spectrum of CDs. (For interpretation of the references to colour in this figure legend, the reader is referred to the web version of this article.)



**Fig. 2.** TEM and corresponding HRTEM images of as prepared CDs/CdS composites with different morphologies: (a, e) CDs/CdS-R, (b, f) CDs/CdS-S, (c, g) CDs/CdS-N and (d, h) CDs/CdS-I.

peaks for (002) plane of CdS in the same locations.

The pore structure and surface areas of as-prepared composite photocatalysts were investigated by the nitrogen adsorption–desorption measurements. **Figs. 4b** and S9 present the nitrogen adsorption–desorption isotherms and the corresponding pore-size distribution curves, respectively. Generally, the  $N_2$ -sorption isotherms can be ascertained as type IV (IUPAC classification), implying the presence of mesopores (2–50 nm). The isotherm of the catalysts has one hysteresis loop defined as H3, directly indicating unimodal pore-size distribution across the mesopore region (2–50 nm). The slit-like pores are due to the aggregation of catalyst nanoparticles. The specific surface areas calculated from the Barrett-Joyner-Halenda (BJH) methods are

listed in **Table 1**. In short, CDs/CdS-S has the highest specific surface area while CDs/CdS-I the lowest; simultaneously, CDs/CdS-R and CDs/CdS-N have similar specific surface area falling between. As a rule, a higher specific surface area is more propitious to catalytic activity [20].

The UV-vis spectra of CdS are provided in **Fig. S10**, in which the absorption edge decreases in the order: CdS-R > CdS-N > CdS-I > CdS-S. Specially, CdS-R exhibits the strongest absorption in the visible light range. The corresponding optical band gaps for CdS samples are calculated from the UV-vis spectra (**Fig. S11**), in which CdS-R possesses the narrowest band gap of 2.30 eV while CdS-N, CdS-I and CdS-S have respectively larger band gaps to be 2.39, 2.41 and 2.40 eV. The absorption intensity and breadth are determined by the

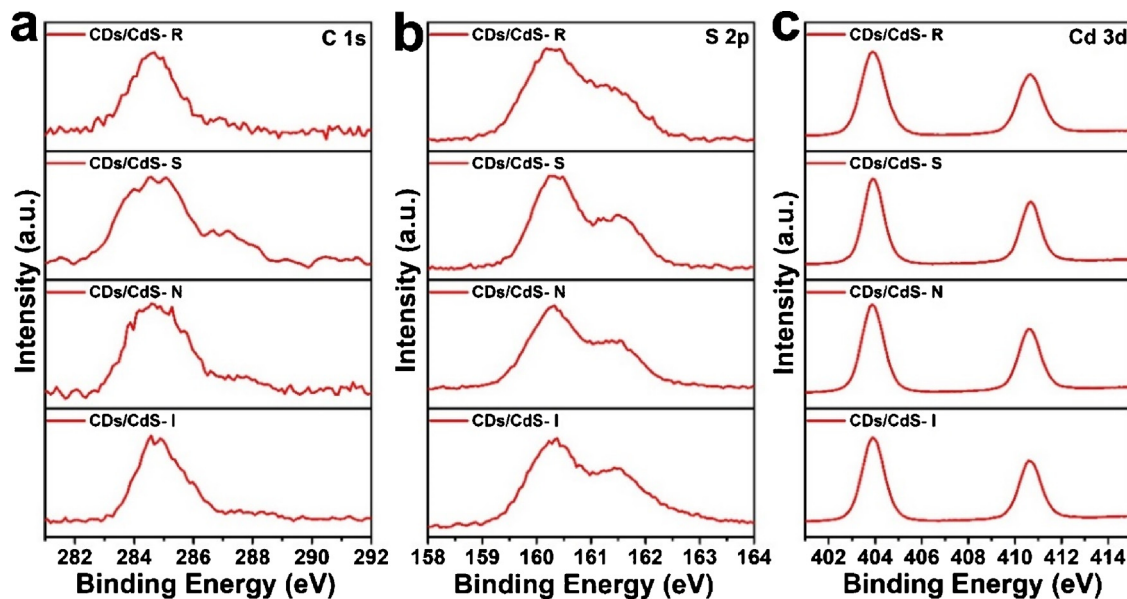


**Fig. 3.** Characterization of the chemical states of CDs/CdS composites (optimal loading content): High-resolution XPS (a) C 1s spectra; (b) S 2p spectra and (c) Cd 3d spectra of CDs/CdS composites.

morphological structure, testifying the importance of morphology study. It turns out some differences for CDs/CdS samples (Fig. 4c), where CDs/CdS-R remains primarily the strongest and the broadest absorption of visible light. The other three photocatalysts have similar absorption in the visible light range, with CDs/CdS-N having a bit broader absorption from 450–500 nm, whereas CDs/CdS-S and CDs/CdS-I show weaker light absorption in range of 400–450 nm. The transformed Tauc-plots in Fig. 4d suggest the optical band gaps of the

composite catalysts. It is clear the composite photocatalysts show nearly the same band gap values with pure phase CdS (within the errors) in the case of the same morphology. The results indicate the introduction of CDs only enhances the light absorption instead of altering the band gap of CdS. Therefore, CDs/CdS composites and the corresponding pure phase CdS samples should conventionally display the same trend in photocatalytic performance.

Since CDs/CdS-S exhibits the highest photocatalytic activity, the

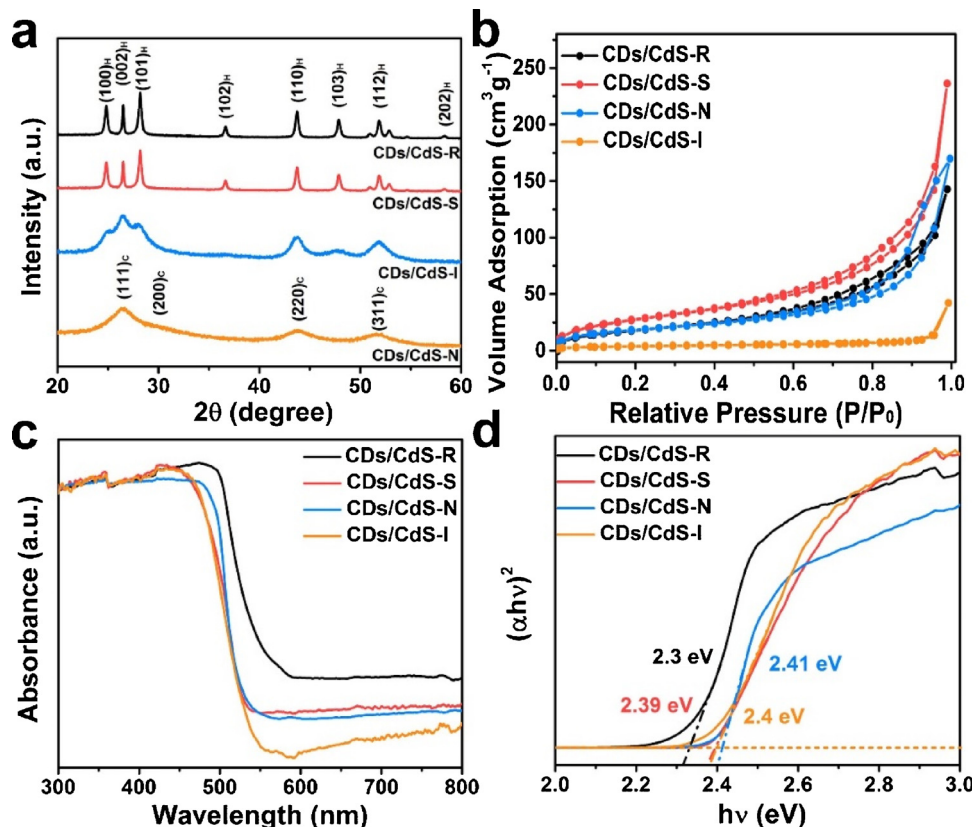


**Fig. 4.** (a) XRD patterns; (b) Nitrogen adsorption-desorption isotherms; (c) UV-vis spectra and (d) the corresponding Tauc plots of CDs/CdS-R, CDs/CdS-S, CDs/CdS-N and CDs/CdS-I.

**Table 1**  
Porous structure parameters of CDs/CdS samples.

Photocatalysts	BET specific surface area ( $\text{m}^2 \text{g}^{-1}$ )	Mean pore diameter (nm)	Pore volume ( $\text{cm}^3 \text{g}^{-1}$ )
CDs/CdS-R	65.25	12.17	0.22
CDs/CdS-S	98.55	14.42	0.37
CDs/CdS-N	65.07	16.78	0.26
CDs/CdS-I	12.81	27.58	0.07

valence band spectra and *Mott-schottky* curves for CdS-S and CDs/CdS-S were measured respectively to verify the energy band structures. The valence band spectra (Fig. S12) of the composites indicate the valence band values are 2.06 and 2.11 V (vs. NHE), from which the conduction band values are calculated to be -0.29 and -0.33 V (vs. NHE) for CdS-S and CDs/CdS-S, respectively. On the other hand, According to the *Mott-schottky* curves (Fig. S13), the slopes are positive that means the samples are n-type semiconductors. For n-type semiconductors, the flat band potential is approximately equal to the valence band value [42]. Therefore, the conduction band values for CdS-S and CDs/CdS-S are measured to be approximately -0.29 and -0.33 V (vs. NHE), consistent with the values from the valence band spectra. These results imply that the incorporation of CDs makes no change to the energy band structure of CdS and the electrons produced by CdS-S and CDs/CdS-S both have the ability to reduce water into  $\text{H}_2$  molecules.

The photocatalytic hydrogen production of the synthesized photocatalysts were tested under visible light irradiation ( $\lambda \geq 420 \text{ nm}$ ) in the presence of 10% lactic acid (volume ratio) via a commercial photocatalytic reaction system (Fig. S14). As shown in Fig. 5a-d, the introduction of CDs into CdS nanocrystals could remarkably enhance the photocatalytic activity. Particularly, a converse decrease in activity would appear over the optimal loading content in that excessive amount of CDs would instead block the absorption of visible light for CdS, which reduces the photocatalytic activity. Fig. 5e illustrates the integrated data from the optimal photocatalysts. When operating in seawater (Fig. 5e), the composite photocatalysts still remain fine photocatalytic activity, which accounts for about 65%, 70%, 55% and 50% of the counterparts in water, respectively. On the contrary, CdS without loading CDs exhibits low activity, which is even worse in seawater

(retain only 30% of the activity in water). The enhancement of the performance of the composites is ascribed to the incorporation of CDs, which not only reduces the overpotential for hydrogen evolution reaction on CDs/CdS composites in comparison with that of bare CdS (Fig. S15), but also works as stable and readily accessible electron acceptors, reducing the distraction from the various ionic components and impurities in seawater. For pure CdS nanocrystals, the photocatalytic activity decreases in the order: CdS-R > CdS-S > CdS-N > CdS-I, which is accordant with the UV/band gap results and structural regularity. However, it is interesting that the composite photocatalysts emerge a little contradictory trend of CDs/CdS-S > CDs/CdS-R > CDs/CdS-N > CDs/CdS-I. This can be attributable to the greatly improved charge separation efficiency and electron transport rate since nanosheet carries more CDs than nanorods. It impresses that CDs/CdS-S composites (0.01  $\text{g}_{\text{CDs}}/\text{g}_{\text{catalyst}}$ ) show a hydrogen production rate of  $268.16 \mu\text{mol h}^{-1}$ , which is 18 times of that of pure CdS-S ( $14.72 \mu\text{mol h}^{-1}$ ). In comparison, CDs/CdS-R (165.47  $\mu\text{mol h}^{-1}$ , 0.005  $\text{g}_{\text{CDs}}/\text{g}_{\text{catalyst}}$ ) is only 4-times higher than that of pure CdS-R ( $32.80 \mu\text{mol h}^{-1}$ ). CDs/CdS-N and CDs/CdS-I also exhibit boosted photocatalytic activity (97.88 and  $32.21 \mu\text{mol h}^{-1}$ , respectively) around 10-times of the corresponding pure CdS ( $9.75$  and  $3.42 \mu\text{mol h}^{-1}$ , respectively), the hydrogen production activities, however, are still relatively low.

AQE is a significant and convincing parameter to appraise the activity of a photocatalyst. Fig. 5f exhibits the calculated AQE values of CDs/CdS (optimal conditions) and CdS at 420 nm. The AQE were calculated to be 15.7%, 19.3%, 8.7% and 3.5% for CDs/CdS-R, CDs/CdS-S, CDs/CdS-N and CDs/CdS-I, accordingly. In contrast, highest AQE value of 2.1% is obtained for CdS-R, yet it is still inferior to the lowest value for CDs/CdS-I. In seawater, CDs/CdS composites maintain about 50%–60% of the AQE measured in water with the highest value of 11.8% for CDs/CdS-S. Additionally, the highest AQE value gained in seawater for CdS is only 0.53% while the lowest is 0.07%, losing 75% of the efficiencies acquired in water.

In total, the AQE values demonstrate the same trend with hydrogen production rate obtained for the photocatalysts, which definitely corroborates the impact of CDs. Certainly, in order to obtain an excellent hybrid photocatalyst, the feasible way is to seek an appropriate coordination between the morphology and cocatalyst. A survey of the photocatalytic seawater splitting performance was also conducted from

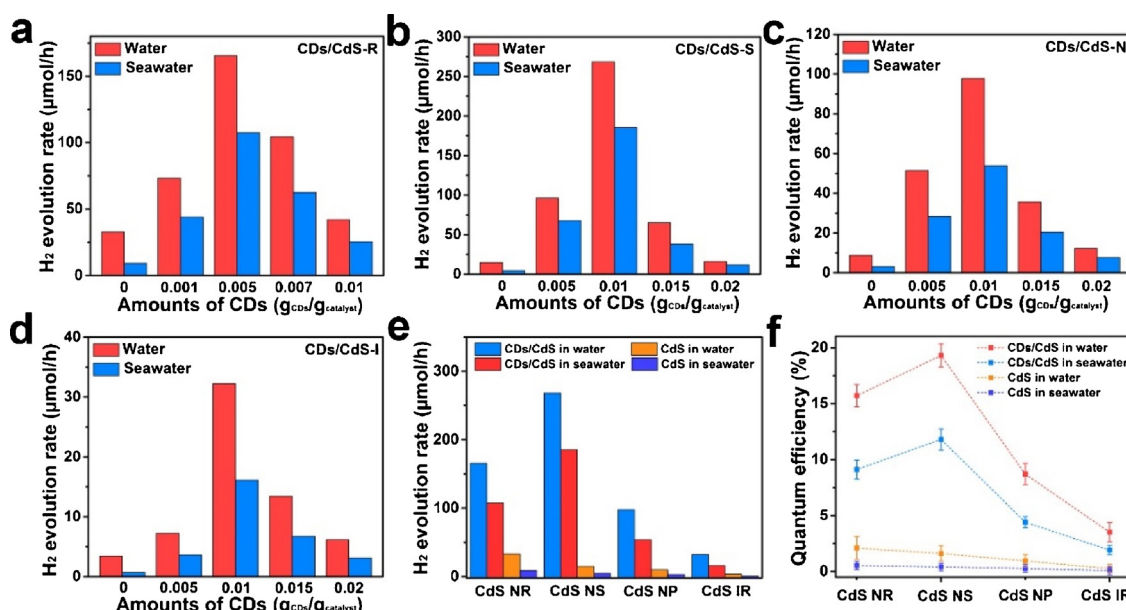
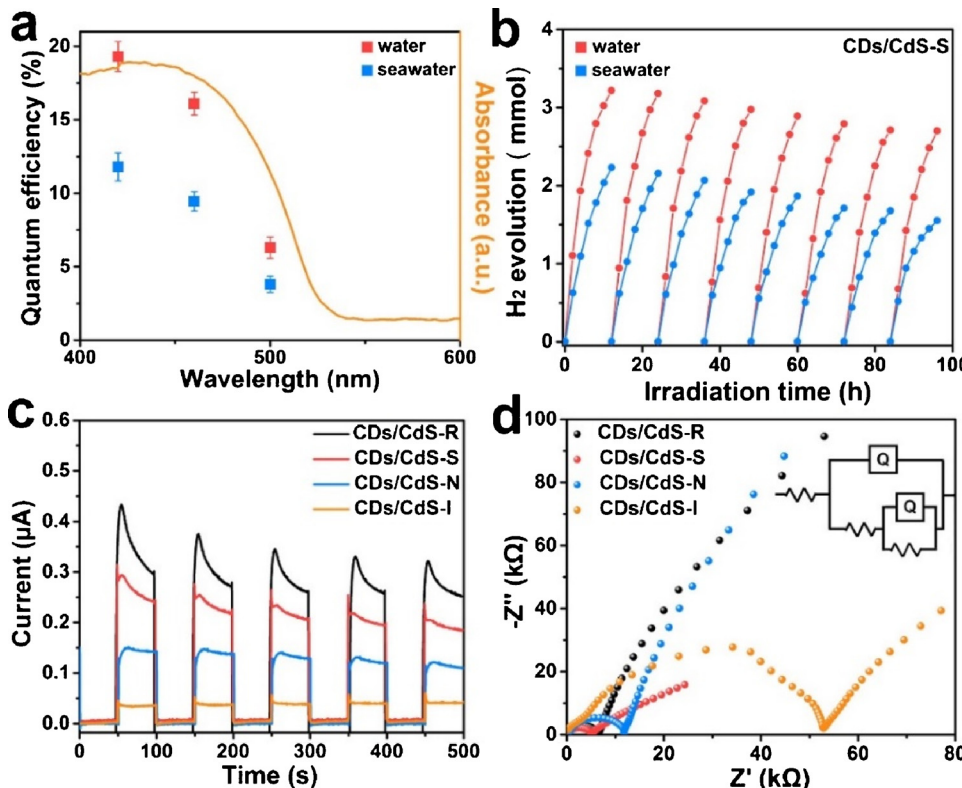


**Fig. 5.** Photocatalytic hydrogen evolution rate of the composite photocatalysts in dependence on morphologies and CDs concentrations in water and seawater. (a) CDs/CdS-R; (b) CDs/CdS-S; (c) CDs/CdS-N; (d) CDs/CdS-I. Comparison of (e) the optimal hydrogen production rate and (f) AQE of CdS and CDs/CdS composites under 420 nm irradiation upon different morphologies.



other works in comparison of our work (Tab. S1), turning out that the activity of our composite photocatalyst is the highest.

For the sake of studying the advantages brought by CDs, a series of experiments were carried out. AQE values as a function of the incident light wavelengths (420, 460 and 500 nm) are illustrated in Fig. 6a, suggesting a desirable correlation with the UV-vis spectrum. AQE decreases with increasing wavelength, and the longest wavelength at 500 nm (close to absorption edge) is still capable of inducing water splitting with an AQE value of 6.3% and 3.8% in water and seawater in accordance. Additionally, stability was tested for CDs/CdS-S (0.01 g<sub>CDs</sub>/g<sub>catalyst</sub>) by reusing for several times. Fig. 6b exemplifies CDs/CdS-S can be reused for 8 times with a decreasing of ~15% in water and ~30% in seawater for photocatalytic activity; in opposite, CdS-S can be only reused for a few times with sharp decrease of activity in water, which even deteriorates in seawater (Fig. S16). The stability is also verified via the XPS S 2p spectra after the respective test cycles (Fig. S17). In Fig. S17a, after 8 times cycling test, only a weak S peak centered at around 163.6 eV is assigned, showing the good stability of CDs/CdS-S. Conversely, the fast deterioration of CdS-S is confirmed by a strong peak affiliated to SO<sub>4</sub><sup>2-</sup> at 168.8 eV and a sub-strong peak belong to S at 163.4 eV (Fig. S17b) [43,44].

Photo-response curves were measured through an intermittent light on-off way under open circuit potential. All CdS samples illustrate a sudden saltation of the photocurrent once irradiated with light, which reveals very fast recombination of the electron-hole pairs (Fig. S18). Note the amelioration of the charge separation efficiency profiting from morphology change is feeble. However, CDs can markedly improve the charge separation efficiency of electron-hole pairs because the saltation of the photo current almost vanishes in CDs/CdS composites, replaced by a gradual decay. On the other hand, as shown in Fig. 6c, the photocurrent decreases in the order: CDs/CdS-R > CDs/CdS-S > CDs/CdS-N > CDs/CdS-I. CDs/CdS-S has weaker photocurrent than CDs/CdS-R but slower decay, not only explaining why CDs/CdS-S shows higher photocatalytic activity, but also strengthening the significance of charge separation efficiency.

Based on Figs. 6d and S19, the charge separation efficiency is

Fig. 6. (a) AQE values of CDs/CdS-S (0.01 g<sub>CDs</sub>/g<sub>catalyst</sub>) gained in water and seawater using 10% lactic acid as scavengers at specific wavelengths (420, 460 and 500 nm) and the fitted UV-vis spectrum. (b) Stability of CDs/CdS-S (0.01 g<sub>CDs</sub>/g<sub>catalyst</sub>) under visible light irradiation using 10% lactic acid as scavengers in water and seawater. (c) Photo-response curves and (d) EIS Nyquist plots (the inset is the fitted equivalent electric circuit) of CDs/CdS composites.

manifestly improved upon the introduction of CDs. As shown in Fig. S19, CdS-S and CdS-R have similar semicircles in EIS Nyquist plots, in which condition the activity mostly depends on the light absorbance (CdS-R is better than CdS-S). CDs/CdS-S displays the smallest semicircle, meaning the charge recombination is more steadily inhibited (Fig. 6d). Fluorescent lifetime spectra of CDs/CdS composites (Fig. S20) show the consistent results with photo-response curves and EIS Nyquist plots, exemplifying the charge recombination rate is more firmly prohibited in CDs/CdS-S. These results have affirmed the role of CDs as fine electron acceptors. CDs have the most significant impact in improving charge separation for CdS nanosheets since CdS nanosheets is more appropriate for uniform anchor of larger amount of CDs (Fig. 7).

These results confirm that the enhancement of light absorption takes slight effect on the photocatalytic activity, and the morphological change brings limited promotion of charge separation efficiency. The charge recombination, however, is effectively prohibited when introducing CDs as cocatalysts that dramatically boosts the photocatalytic activity towards hydrogen production even at a low loading content. The results also exemplify charge separation is the rate determining step during the photocatalytic process of CDs/CdS photocatalysts, which is implicative and instructive towards following work concerning photocatalytic water splitting.

#### 4. Conclusions

In this paper, we demonstrate the synthesis of a series of CDs/CdS composites to assess the influence of CDs for water splitting in water and seawater. We find that the introduction of CDs onto CdS greatly improves the hydrogen production activity and stability, particularly in seawater. The impressive photocatalytic activity and stability are primarily attributable to the function of CDs as cocatalysts, which not only improve the charge separation efficiency, but also stabilize the electrons from the distraction of seawater. Therefore, it would be very favorable to arrive at an adequate consolidation between morphology and cocatalyst for photocatalysts. We hope this work can provide a referable methodology to design high-efficient and low-cost hybrid

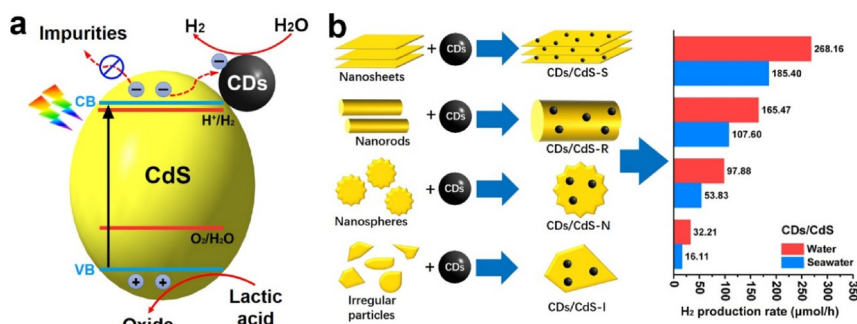


**Fig. 7.** (a) Working mechanism of CDs/CdS composites in seawater and (b) comparison of CDs/CdS composites on account of morphologies and photocatalytic activities.

photocatalysts, hence progressing the step to industrialized hydrogen fuels.

#### Notes

The authors declare no competing financial interest.

#### Acknowledgments

This work is supported by the Collaborative Innovation Center of Suzhou Nano Science and Technology, the National Natural Science Foundation of China (51725204, 51572179, 21471106, 21771132, 21501126), the Natural Science Foundation of Jiangsu Province (BK20161216), the 111 Project and a project funded by the Priority Academic Program Development of Jiangsu Higher Education Institutions (PAPD).

#### Appendix A. Supplementary data

Supplementary material related to this article can be found, in the online version, at doi:<https://doi.org/10.1016/j.apcatb.2018.09.096>.

#### References

- [1] C. Acar, I. Dincer, C. Zamfirescu, *Int. J. Energy Res.* 38 (2014) 1903–1920.
- [2] A. Fujishima, K. Honda, *Nature* 238 (1972) 37–38.
- [3] A. Kudo, Y. Misaki, *Chem. Soc. Rev.* 38 (2009) 253–278.
- [4] H. Ahmad, S.K. Kamarudin, L.J. Minggu, M. Kassim, *Renew. Sustain. Energy Rev.* 43 (2015) 599–610.
- [5] S.J.A. Moniz, S.A. Shevlin, D.J. Martin, Z.-X. Guo, J. Tang, *Energy Environ. Sci.* 8 (2015) 731–759.
- [6] X. Chen, S. Shen, L. Guo, S.S. Mao, *Chem. Rev.* 110 (2010) 6503–6570.
- [7] T. Hisatomi, J. Kubota, K. Domen, *Chem. Soc. Rev.* 43 (2014) 7520–7535.
- [8] S. Cao, J. Low, J. Yu, M. Jaroniec, *Adv. Mater.* 27 (2015) 2150–2176.
- [9] K. Maeda, J. Photochem. Photobiol. C: Photochem. Rev. 12 (2011) 237–268.
- [10] T. Jafari, E. Moharreri, A. Amin, R. Miao, W. Song, S. Suib, *Molecules* 21 (2016) 900.
- [11] H. Li, W. Tu, Y. Zhou, Z. Zou, *Adv. Sci.* 3 (2016) 1500389.
- [12] H. Li, Y. Zhou, W. Tu, J. Ye, Z. Zou, *Adv. Funct. Mater.* 25 (2015) 998–1013.
- [13] X. Zong, H. Yan, G. Wu, G. Ma, F. Wen, L. Wang, C. Li, *J. Am. Chem. Soc.* 130 (2008) 7176–7177.
- [14] H. Yan, J. Yang, G. Ma, G. Wu, X. Zong, Z. Lei, J. Shi, C. Li, *J. Catal.* 266 (2009) 165–168.
- [15] S. Xiong, B. Xi, Y. Qian, *J. Phys. Chem. C* 114 (2010) 14029–14035.
- [16] X. Wang, M. Liu, Z. Zhou, L. Guo, *J. Phys. Chem. C* 119 (2015) 20555–20560.
- [17] D. Lang, Q. Xiang, G. Qiu, X. Feng, F. Liu, *Dalton Trans.* 43 (2014) 7245–7253.
- [18] Y. Lei, C. Yang, J. Hou, F. Wang, S. Min, X. Ma, Z. Jin, J. Xu, G. Lu, K.-W. Huang, *Appl. Catal. B: Environ.* 216 (2017) 59–69.
- [19] F. Vaquero, R.M. Navarro, J.L.G. Fierro, *Appl. Catal. B: Environ.* 203 (2017) 753–767.
- [20] J. Yu, Y. Yu, P. Zhou, W. Xiao, B. Cheng, *Appl. Catal. B: Environ.* 156–157 (2014) 184–191.
- [21] J. Ran, J. Zhang, J. Yu, M. Jaroniec, S.Z. Qiao, *Chem. Soc. Rev.* 43 (2014) 7787–7812.
- [22] Y. Xu, R. Xu, *Appl. Surf. Sci.* 351 (2015) 779–793.
- [23] J. Yang, D. Wang, H. Han, C. Li, *Acc. Chem. Res.* 46 (2013) 1900–1909.
- [24] Y. Li, X. Wei, X. Yan, J. Cai, A. Zhou, M. Yang, K. Liu, *Phys. Chem. Chem. Phys.* 18 (2016) 10255–10261.
- [25] Y. Li, R. Wang, H. Li, X. Wei, J. Feng, K. Liu, Y. Dang, A. Zhou, *J. Phys. Chem. C* 119 (2015) 20283–20292.
- [26] A.-J. Simamora, T.-L. Hsiung, F.-C. Chang, T.-C. Yang, C.-Y. Liao, H.P. Wang, *Int. J. Hydrogen Energy* 37 (2012) 13855–13858.
- [27] W. Luo, Z. Yang, Z. Li, J. Zhang, J. Liu, Z. Zhao, Z. Wang, S. Yan, T. Yu, Z. Zou, *Energy Environ. Sci.* 4 (2011) 4046.
- [28] S.-H. Hsu, J. Miao, L. Zhang, J. Gao, H. Wang, H. Tao, S.-F. Hung, A. Vasileff, S.Z. Qiao, B. Liu, *Adv. Mater.* 30 (2018) 1707261.
- [29] Y. Li, J. Feng, H. Li, X. Wei, R. Wang, A. Zhou, *Int. J. Hydrogen Energy* 41 (2016) 4096–4105.
- [30] H. Li, Z. Kang, Y. Liu, S.-T. Lee, *J. Mater. Chem.* 22 (2012) 24230.
- [31] H. Ming, Z. Ma, Y. Liu, K. Pan, H. Yu, F. Wang, Z. Kang, *Dalton Trans.* 41 (2012) 9526.
- [32] C. Zhu, Y. Fu, C. Liu, Y. Liu, L. Hu, J. Liu, I. Bello, H. Li, N. Liu, S. Guo, H. Huang, Y. Lifshitz, S.-T. Lee, Z. Kang, *Adv. Mater.* 29 (2017) 1701399.
- [33] J. Liu, Y. Liu, N. Liu, Y. Han, X. Zhang, H. Huang, Y. Lifshitz, S.-T. Lee, J. Zhong, Z. Kang, *Science* 347 (2015) 967–970.
- [34] C. Zhu, C. Liu, Y. Zhou, Y. Fu, S. Guo, H. Li, S. Zhao, H. Huang, Y. Liu, Z. Kang, *Appl. Catal. B: Environ.* 216 (2017) 114–121.
- [35] X. Wu, C. Zhu, L. Wang, S. Guo, Y. Zhang, H. Li, H. Huang, Y. Liu, J. Tang, Z. Kang, *ACS Catal.* 7 (2017) 1637–1645.
- [36] H. Yu, R. Shi, Y. Zhao, G.I.N. Waterhouse, L.-Z. Wu, C.-H. Tung, T. Zhang, *Adv. Mater.* 28 (2016) 9454–9477.
- [37] G. Xie, K. Zhang, B. Guo, Q. Liu, L. Fang, J.R. Gong, *Adv. Mater.* 25 (2013) 3820–3839.
- [38] Q. Li, B. Guo, J. Yu, J. Ran, B. Zhang, H. Yan, J.R. Gong, *J. Am. Chem. Soc.* 133 (2011) 10878–10884.
- [39] S. Ma, J. Xie, J. Wen, K. He, X. Li, W. Liu, X. Zhang, *Appl. Surf. Sci.* 391 (2017) 580–591.
- [40] J. Yang, J. Wang, X. Li, D. Wang, H. Song, *Catal. Sci. Technol.* 6 (2016) 4525–4534.
- [41] A. Ye, W. Fan, Q. Zhang, W. Deng, Y. Wang, *Catal. Sci. Technol.* 2 (2012) 969.
- [42] H. Yan, J. Yang, G. Ma, G. Wu, X. Zong, Z. Lei, J. Shi, C. Li, *J. Catal.* 266 (2009) 165–168.
- [43] D. Meissner, C. Benndorf, R. Memming, *Appl. Surf. Sci.* 27 (1987) 423–436.
- [44] D. Oyetunde, M. Afzaal, M.A. Vincent, I.H. Hillier, P. O'Brien, *Inorg. Chem.* 50 (2011) 2052–2054.